Ocean Modelling 124 (2018) 1–15

Contents lists available at ScienceDirect

Ocean Modelling

journal homepage: www.elsevier.com/locate/ocemod

Parameterized and resolved Southern Ocean eddy compensation

Mads B. Poulsen*, Markus Jochum, Roman Nuterman

Niels Bohr Institute, University of Copenhagen, Juliane Maries Vej 30, Copenhagen 2100, Denmark

ARTICLE INFO

Keywords:
Southern Ocean
Eddy compensation
Parameterized sensitivity

ABSTRACT

The ability to parameterize Southern Ocean eddy effects in a forced coarse resolution ocean general circulation model is assessed. The transient model response to a suite of different Southern Ocean wind stress forcing perturbations is presented and compared to identical experiments performed with the same model in 0.1° eddy-resolving resolution. With forcing of present-day wind stress magnitude and a thickness diffusivity formulated in terms of the local stratification, it is shown that the Southern Ocean residual meridional overturning circulation in the two models is different in structure and magnitude. It is found that the difference in the upper overturning cell is primarily explained by an overly strong subsurface flow in the parameterized eddy-induced circulation while the difference in the lower cell is mainly ascribed to the mean-flow overturning. With a zonally constant decrease of the zonal wind stress by 50% we show that the absolute decrease in the overturning circulation is insensitive to model resolution, and that the meridional isopycnal slope is relaxed in both models. The agreement between the models is not reproduced by a 50% wind stress increase, where the high resolution overturning decreases by 20%, but increases by 100% in the coarse resolution model. It is demonstrated that this difference is explained by changes in surface buoyancy forcing due to a reduced Antarctic sea ice cover, which strongly modulate the overturning response and ocean stratification. We conclude that the parameterized eddies are able to mimic the transient response to altered wind stress in the high resolution model, but partly misrepresent the unperturbed Southern Ocean meridional overturning circulation and associated heat transports.

1. Introduction

The outcropping isopycnals of the Southern Ocean provide an important adiabatic pathway for the meridional overturning circulation and hence aid the ventilation of the deep ocean (Marshall and Speer, 2012). Together with the zonally unblocked Antarctic Circumpolar Current, the Southern Ocean thus plays a central role in the modern view of the ocean general circulation (Gnanadesikan, 1999; Thompson et al., 2016), the global carbon cycle (Sigman and Boyle, 2000; Le Quéré et al., 2007; Bronselaer et al., 2016), ocean heat uptake (Marshall and Zanna, 2014) and the exchange of tracers between the major ocean basins (Thompson, 2008). The southern hemisphere westerlies are a key driving force of the circulation (e.g. Toggweiler and Samuels, 1995; Tansley and Marshall, 2001) and these have been subject to an intensification and poleward shift throughout the last several decades as a result of ozone depletion and anthropogenic emission of carbon dioxide (Thompson and Solomon, 2002; Marshall, 2003). A fundamental question is what implication the wind stress changes have on the global circulation and climate, and whether the relevant physics is faithfully represented in state-of-the-art climate models to allow for meaningful predictions of the response.

In this respect, the mesoscale eddy field in the Southern Ocean (e.g. Frenger et al., 2015) has proven to have a leading order influence on the local dynamics. Ocean models of varying complexity and basin geometry, but with an explicitly resolved eddy field, have demonstrated that a limit exists in which the time-mean transport of a circumpolar current becomes independent of the strength of the overlying zonal wind stress (Hogg and Blundell, 2006; Nadeau and Straub, 2009; Munday et al., 2013; Marshall et al., 2017). Beyond this limit additional momentum input to the surface ocean by the winds mainly fuel a stronger eddy field through baroclinic instability, which facilitates a vertical momentum transfer to the ocean floor and dissipation by form drag (Munk and Palmén, 1951; Johnson and Bryden, 1989), instead of accelerating the current. Recent observations from the Southern Ocean have shown that the isopycnal slope, and hence the baroclinic transport of the Antarctic Circumpolar Current, has indeed been insensitive to the wind stress changes (Böning et al., 2008) while the surface kinetic energy has increased (Hogg et al., 2015), supporting the model results and the notion that the Southern Ocean is in the so-called state of eddy saturation.

Contemporary residual-mean theory also emphasizes the role of mesoscale eddies in setting the strength of the upper cell of the

* Corresponding author.
E-mail address: mads.poulsen@nbi.ku.dk (M.B. Poulsen).

https://doi.org/10.1016/j.ocemod.2018.01.008
Received 7 April 2017; Received in revised form 17 January 2018; Accepted 30 January 2018
Available online 01 February 2018

meridional overturning in the Southern Ocean. Here they compensate the effect of a wind-driven northward Ekman flow anomaly through an oppositely directed flow akin to a Stokes drift (referred to as eddy compensation, see e.g. Marshall and Radko (2003)). The results from models with explicit eddies show that this is indeed the case (Hallberg and Gnanadesikan, 2006), but also that the sensitivity of the overturning circulation remains non-zero to a wind stress strength that is several times greater than the present day magnitude, unlike the behavior of the zonal transport (Munday et al., 2013). Using an idealized primitive equation model at various eddying resolutions, Morrison and Hogg (2013) likewise demonstrate the sensitivity difference between the zonal and meridional circulation to the zonal wind stress. They argue that the sensitivity difference arises because eddy compensation is a depth-dependent metric, whereas eddy saturation is depth-integrated and thus camouflages potentially higher local sensitivities in the vertical shear of the horizontal velocity field.

In a recent high-resolution coupled model experiment run for two model decades, Bishop et al. (2016) shows that the upper cell of the residual overturning increases in magnitude by 39% to a zonally constant 50% increase of the Southern Ocean zonal wind stress, and that the mean Drake Passage transport changes by 6% only. The degree of compensation and saturation that should be expected on a longer time scale is however still unclear as computational cost limits sufficiently long integrations of comprehensive high resolution ocean models. Moreover, the non-local response of the Atlantic meridional overturning circulation to a Southern Ocean wind stress change is continuously debated. For example, it has been suggested that models with idealized basin geometry do not capture the changes in diapycnal upwelling in the Pacific Ocean. Since this diabatic pathway is also able to provide the necessary closure for the meridional overturning circulation, these models potentially overestimate the role of the Southern Ocean winds (Jochum and Eden, 2015).

The results from eddy-resolving ocean models, despite their simplifications and shortcomings, have questioned the ability of coarse resolution ocean models to represent the eddy effect on the large-scale flow in a wind stress change scenario. Most climate models use the Gent–McWilliams parameterization (Gent and McWilliams, 1990; Gent et al., 1995) to model baroclinic instability and along-isopycnal eddy mixing in the interior ocean, and rely on the assumption that the strength of baroclinic instability is proportional to the isopycnal slope. Comparison studies have shown that when the proportionality parameter in the eddy down-gradient closure, the thickness diffusivity, is a constant, the zonal transport cannot possibly eddy saturate and the meridional circulation is too sensitive to wind stress changes (Hallberg and Gnanadesikan, 2006; Munday et al., 2013). When the eddy diffusivity is allowed to vary in space and time as function of the stratification (Ferreira et al., 2005; Danabasoglu and Marshall, 2007), the transport through Drake Passage shows a less sensitive relationship to the zonal wind stress (Gent and Danabasoglu, 2011). However, the change in the residual overturning still varies considerably among models subject to the same wind stress increase (Farneti et al., 2015), which complicates an assessment of the parameterized eddy effect.

Both Bitz and Polvani (2012) and Bryan et al. (2014) compare climate change experiments between a fully coupled coarse resolution model, using above parameterization, and an identical eddy-resolving model. The model solutions in the study by Bryan et al. (2014) show that the poleward eddy heat transport between 60°S and 50°S increases following an increase in the zonal wind stress in their low resolution model setup, whereas the high resolution model finds a response of opposite sign. Bitz and Polvani (2012) report similar model responses, where the resolved eddies contribute substantially less to the change in poleward heat transport compared to the parameterized eddies. While these results suggest that the parameterized eddies respond oppositely or overly strong to a wind stress change, ambiguity on the performance of the eddy parameterization still remains, because the modelled wind stress changes are dependent on the background climate. This is not necessarily the same at different model resolution, exemplified by Bryan et al. (2014), where differences in Antarctic sea ice thickness influence the modelled climate response. In addition, an increasing body of literature has shown that the strength of the Antarctic Circumpolar Current and the position of its fronts is sensitive to the spatial structure and strength of the wind stress field (Sallée et al., 2008; Morrow et al., 2010; Mazloff, 2012; Dufour et al., 2012; Zika et al., 2013; Langlais et al., 2015). The compilation of these results suggest a return to simpler general circulation model experimental setups with a complete control on the applied wind stress to elucidate the nature of the response.

In the present study we present simulations from the second version of the Parallel Ocean Program (POP) model configured at a horizontal resolution of 1° and 0.1°, the former employing a state-of-the-art eddy parameterization, forced with different prescribed Southern Ocean wind stress scenarios in an attempt to evaluate the performance of parameterized eddies. The results presented here indicate that the parameterized eddy-induced meridional circulation cancel the wind-driven overturning differently than the eddy-resolving model when forced with present day winds. Despite differences in the background ocean state we demonstrate that the two models respond similarly to wind stress perturbations, but note that the model comparison is not straightforward as changes in buoyancy forcing and sea ice cover are able to drive a complex model response. The latter point raises the question to what extent the current concept of eddy compensation is applicable to complex models.

2. Model description, experimental setup and spin-up assessment

We use the Community Earth System Model (CESM) with an active ocean and sea ice model on a global domain with realistic bottom topography with prescribed meteorological boundary conditions. The ocean and sea ice models share the same grid, and the solution of the governing equations is sought using two different horizontal grid resolutions; a tri-polar 0.1° grid, with the meridional grid spacing proportional to the cosine of latitude, and a dipole 1° grid that also has a meridional grid discretization that varies with latitude, with a latitudinal grid spacing of $\sim 0.5°$ in the Southern Ocean. The vertical axis that belongs to the first grid is resolved by 62 z-coordinate levels, with the distance of separation increasing monotonically with depth, and has a partial bottom cell representation in accord with the ETOPO2v2 bathymetry product. The coarse resolution grid holds 60 levels in the vertical and with no partial bottom cells. The dynamical core of the ocean model is the same for both grid resolutions and is documented in Smith et al. (2010), except for the treatment of motion on the mesoscale, which is outlined in the next paragraph. For further information on the grid layouts and aspects of the control integration of the fully coupled models, the reader is referred to Gent et al. (2011) and Small et al. (2014) with respect to the coarse and the fine resolution model, respectively. The prescribed atmosphere used in this study is given by the normal year forcing fields from the second version of the Coordinated Ocean Research Experiment (CORE.v2.NYF, Large and Yeager, 2008), compiled from atmospheric reanalysis and observations, and the fields have a temporal resolution of six hours and repeat themselves after one model year exactly.

Ideally the model solution that evolves on the 0.1° grid should be subject to motion on a characteristic length scale on the order of the first baroclinic Rossby radius (Chelton et al., 1998) and no mesoscale eddy parameterization is therefore enabled. The isopycnal tracer diffusion is likewise disabled, but a biharmonic operator is implemented to represent lateral mixing by subgrid-scale processes that remain unresolved (Bryan and Bachman, 2015). Ocean mesoscale eddies are not explicitly resolved on the 1° grid and are parameterized in the interior ocean using the Gent and McWilliams (1990) isopycnal mixing formulation with the spatiotemporal thickness diffusivity proposed by Ferreira et al. (2005). This choice of the eddy transfer coefficient

ensures that it is surface intensified, in alignment with previous studies, and has shown to improve the model solution with respect to observations of the Southern Ocean density structure and leads to a greater cancellation between the wind-driven and eddy-induced Southern Ocean meridional cells (Danabasoglu and Marshall, 2007; Farneti et al., 2015). As default in POP, the parameterized ocean interior eddy fluxes are modified towards the surface boundary layer in accord with Ferrari et al. (2008), where diabatic eddy fluxes are aligned with the surface ocean. Of additional relevance to this study, convective instability is handled implicitly in both models; that is, the local vertical diffusivity is increased by several orders of magnitude when the water column is statically unstable. During statically stable conditions, the vertical mixing is parameterized as in Large et al. (1994).

The model on the 1° grid was initialized from a state of rest and the property fields from the Polar Science Center Hydrographic Climatology (Steele et al., 2001), and a control simulation (labelled Ccont) of 300 model years was integrated forward with the default wind stress, denoted by $\tau_0 = (\tau_0^\phi, \tau_0^\theta)$. The control simulation with the 0.1° model (labelled Hcont), was also initialized from rest but the initial conditions to the salt and temperature fields were instead provided by the World Ocean Circulation Experiment Hydrographic Climatology (Gouretski and Koltermann, 2004). The first 16 years of Hcont were conducted at the National Center for Atmospheric Research and is described in detail in Bryan and Bachman (2015). The model run was hereafter adopted by the authors and integrated additionally ten years forward in time to reach a total Hcont length of 26 years.

Several wind stress change experiments were branched off from the last year of both Ccont and Hcont with the zonal wind stress in the Southern Ocean subject to

$$\tau^\phi(\phi, \theta, t) = \tau_0^\phi(\phi, \theta, t)F(\theta), \tag{1}$$

where τ^ϕ is the perturbed zonal wind stress. F is a time-invariant perturbation that has a zonally constant structure expressed by

$$F(\theta) = \begin{cases} F_0, & \text{for } \theta \leq 35°\text{S} \\ \dfrac{a\pi}{180°}\theta + b, & \text{for } 35°\text{ S} < \theta < 25°\text{S} \\ 1, & \text{otherwise,} \end{cases} \tag{2}$$

and it is understood that θ increases northward. Here F_0 is the perturbation factor and a and b were chosen such that the linear decrease of the perturbation with latitude matches F_0 at $\theta = 35°$S and unity at 25°S. This is the same perturbation that was used in the coupled model studies by Gent and Danabasoglu (2011), Jochum and Eden (2015) and Bishop et al. (2016).

Table 1 summaries the suite of wind stress experiments presented in this paper, as well as their abbreviations, and provides the coefficients specific to the applied perturbations. A 50% wind stress increase and decrease experiment (blue and magenta line, upper left panel of Fig. 1) were extended from the end of the high resolution control simulation (labelled Htau15 and Htau05, respectively), both of 16 years duration. The output from Htau15 and Htau05, as well as the last year from Hcont, was stored as three-day mean fields and subsequently reduced to monthly means to fit the purpose of this study. Identical perturbations to the wind stress field were conducted with the coarse resolution model, the experiments labelled Ctau05 and Ctau15, both of 100 model year duration. As will become evident later in the reading of the present study, the wind stress increase perturbation pushes the state of the marginal seas of the Southern Ocean towards a state that favors deep convection, which influences the overturning response in Htau15. To emphasize this point, a double wind stress increase experiment (green line, upper left panel of Fig. 1) with the 1° model (labelled Ctau20) is performed, also of 100 year duration.

Table 1
List of experiments and their characteristics. The acronym for each of the different experiments is provided in the leftmost column. F_0, a and b are the coefficients that enter in the perturbation given by Eq. (2).

Exp.	Resolution	F_0	a	b	Duration [years]
Hcont	0.1°	1.0	0.0	1.0	26
Htau05	0.1°	0.5	2.941	2.294	16
Htau15	0.1°	1.5	−2.941	−0.294	16
Ccont	1°	1.0	0.0	1.0	300
Ctau05	1°	0.5	2.941	2.294	100
Ctau15	1°	1.5	−2.941	−0.294	100
Ctau20	1°	2.0	−5.882	−1.588	100

Throughout this study, and unless otherwise stated, the analysis of Ccont and Hcont is conducted on the ten years that lead up to the application of the wind stress perturbation. That is, year 16 to 25 for Hcont and year 290 to 299 for Ccont. The analysis of the high resolution wind stress experiments is focussed on the last ten years, the time span between year 33 and 42, and the corresponding time span for the coarse resolution experiments is between year 307 and 316. The time-mean of Ctau20 is taken between model year 313 to 322, shifted by six years relative to Ctau15, due to a difference in the timing of the onset of deep convection relative to Htau15.

The black curve in the upper left panel of Fig. 1 shows the annual mean zonally-averaged zonal wind stress profile that arises from the unperturbed forcing field, and the peak wind stress is smaller by approximately 25% than what is found in the coupled model configuration (Gent and Danabasoglu, 2011; Bryan et al., 2014; Bishop et al., 2016). Comparing the time-mean Drake Passage transport profile from Hcont to the corresponding profile from Ccont, it is seen that there is an overall good agreement between the models in terms of the vertical velocity shear (upper right panel, Fig. 1). The depth-integrated volume transport of Hcont and Ccont yields similar time-mean Drake Passage transports of 133 Sv and 136 Sv, respectively, and compares well with the 134 ± 27 Sv full-depth observational estimate reviewed by Cunningham et al. (2003). The more recent estimate of 141 ± 13 Sv by Koenig et al. (2014), based on satellite altimetry and mooring data, agrees with the presented model solutions as well, although the 173 ± 11 Sv estimate by Donohue et al. (2016), which additionally includes a barotropic contribution from resolved near-bottom currents, suggests that the modelled Drake Passage transport in both models is too low.

The winter-mean boundary layer depth simulated in the two models, defined in Large et al. (1994), is seen in the lower row of plots in Fig. 1, as well as the 15% austral winter-mean (July-August-September) sea ice concentration isoline from the model (white line) and from the Special Sensor Microwave Imager observations (black line, Comiso (2000)). The boundary layer depth of Ccont (left) in general agrees with Hcont (right) on the large scale, but Hcont also possesses several local maxima, of which some occur in proximity of topographic obstacles, and has a deeper boundary layer in the path of the Antarctic Circumpolar Current in the Indian Ocean sector. Hcont also displays a deeper boundary layer close to the coast of Antarctica, especially in the Weddell Sea, which is the signature of dense water formation. The observed extent of the winter sea ice cover in general compares well with the two model simulations, though with a misrepresentation in the Pacific sector in Ccont, and a too large extent in Hcont to the east of Drake Passage and south of Australia.

The computational costs of the 0.1° model made it difficult to integrate the high resolution simulations closer to their equilibrium solution given our resources. The total sum of 42 high resolution model years required more than a year to complete on 4096 cores of the BlueGene supercomputer located in Jülich, Germany, and exhausted our resources. Model drift therefore remains, and it is here examined in Hcont to identify the fraction of the model response presented in the results section which is due to model drift.

The upper left panel of Fig. 2 displays the evolution of the horizontally averaged potential temperature field of the Southern Ocean in Hcont from model year 16 to 25. On decadal time-scale, as is the

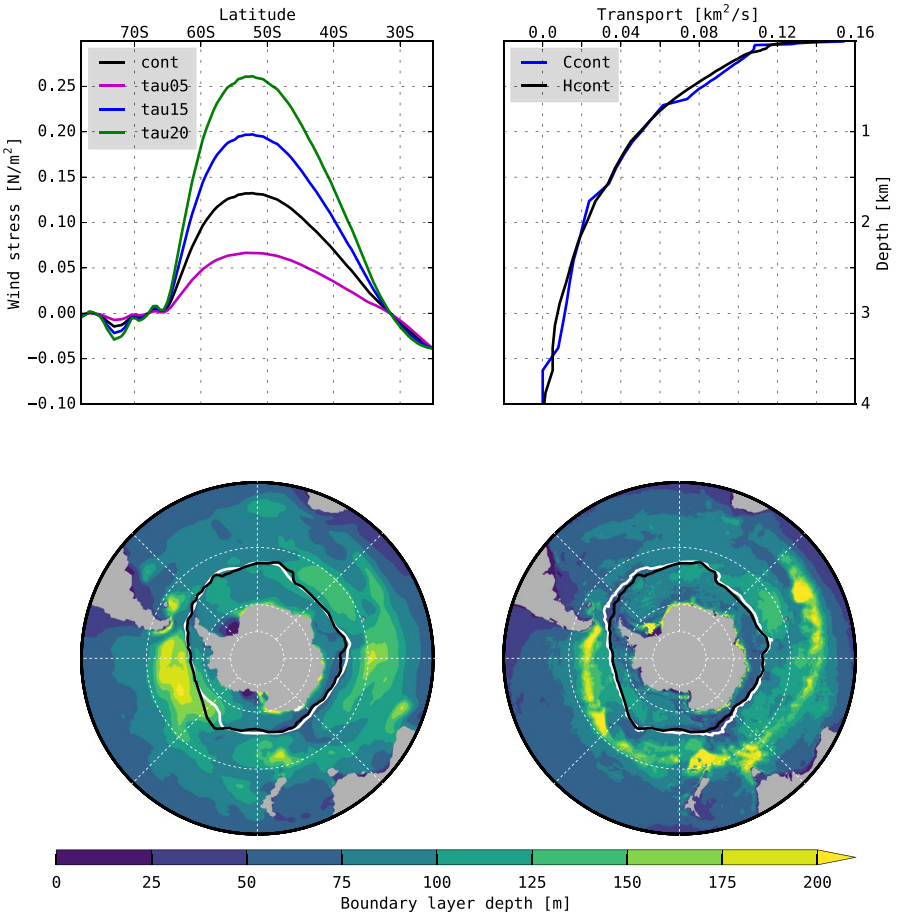

Fig. 1. The upper left panel shows the zonal average of the annual mean zonal wind stress fields from the different experiments. The black, magenta, blue and green lines are from the control, 50% wind stress decrease, 50% increase and 100% increase, respectively. Units are in N/m^2. The upper right panel is the ten-year mean transport profiles from the Drake Passage. The blue line is from Ccont (year 290 − 299) and the black line is from Hcont (year 16 − 25). The units are in km^2/s. The lower left panel displays the ten-year mean winter (July-August-September) boundary layer depth from Ccont. The white and black solid lines are the 15% July-August-September sea ice concentration contour from the model and from observations, respectively. The lower right panel shows the same as the lower left panel, but for Hcont. Color interval is 25 m. (For interpretation of the references to colour in this figure legend, the reader is referred to the web version of this article.)

interest of the present study, significant drift is present between 1000 m and 400 m depth. The Southern Ocean warms at a rate about 0.2 °C/decade at 600 m depth, and is of the same magnitude and location as the warming trend presented by Small et al. (2014), who examine the model in its coupled configuration. The abyssal ocean also warms, but equilibrates the slowest and does not drift much on the decadal timescale. For comparison, Ccont, which is integrated much further towards equilibrium, warms by approx. 0.003 °C/decade only at 600 m depth, evaluated between model year 290 and 299.

The ten-year mean temperature profiles of both Ccont (blue) and Hcont (black) are shown in the upper right panel. The profiles in the deep ocean match quite well, but Hcont is seen to be warmer by ∼ 1 °C than Ccont above 1km depth, and the difference becomes bigger as time progress due to the model drift. However, the meridional density gradient across the Southern ocean does not appear to be affected by the difference in temperature stratification and the model drift, as is indirectly inferred from the time series of the Drake Passage transport in the lower panel of Fig. 2. The strength of the Southern Ocean meridional overturning circulation also does not appear to drift, which is discussed in greater detail in Section 4, and shown in Fig. 5. We thus

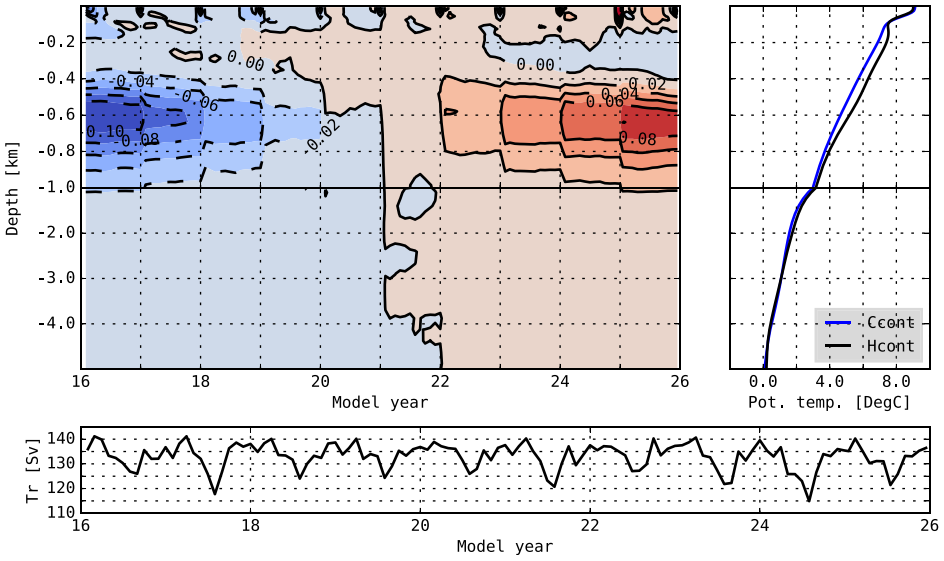

Fig. 2. The upper left panel displays the temporal evolution of the horizontally-averaged potential temperature anomaly south of 30°S for Hcont between model year 16 and 25. The seasonal cycle has been removed. Dashed and solid contours are negative and positive, respectively, and the contour interval is 0.02 °C. The upper right panel shows the ten-year mean temperature profile for both Ccont (blue) and Hcont (black). The lower panel shows the Drake Passage transport time series from the last ten years of Hcont. (For interpretation of the references to colour in this figure legend, the reader is referred to the web version of this article.)

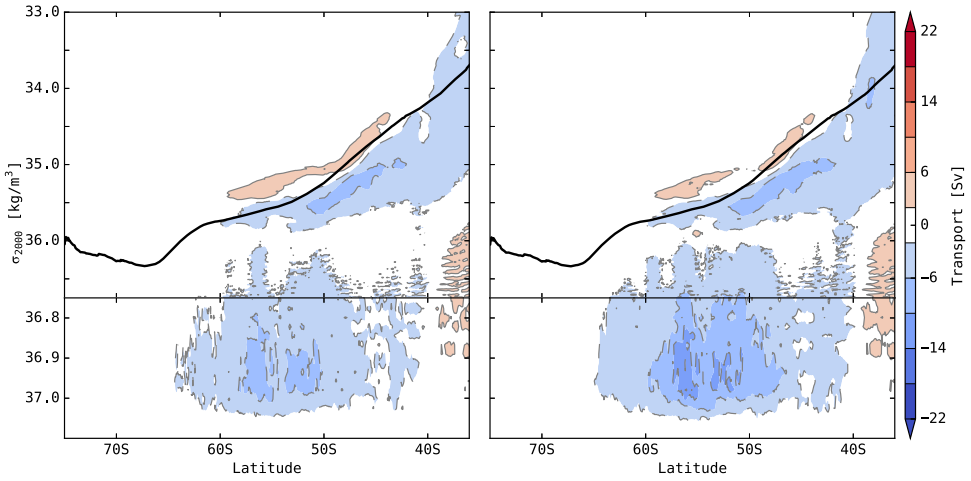

Fig. 3. The left panel displays the ten-year mean eddy-induced overturning circulation ψ_I^* from the Htau05 experiment calculated with monthly-mean output fields. The right panel shows the same as the left panel, but calculated using three-day mean output. The time span is from model year 33 to 42. Units are in Sv, 1 Sv $\equiv 1 \times 10^6$ m^3/s, and color interval is 4 Sv. The black solid line is the zonal mean of the time-mean surface potential density field, and provides an approximate measure of the surface ocean. Note the non-linear y-axis.

consider a comparison between the high and coarse resolution model meaningful, but the shortness and drift of the high resolution model integrations is a caveat of the present study that should be kept in mind.

3. Decomposition of the meridional overturning circulation

To avoid the representation of artificial diapycnal flows in the Southern Ocean, the analysis of the meridional overturning circulation is here performed in density coordinates, in accord with previous related studies (e.g. Hallberg and Gnanadesikan, 2006; Munday et al., 2013; Bishop et al., 2016). When remapped to vertical coordinates, such overturning circulation is found to respect the adiabatic nature of the interior ocean, with streamlines approximately aligned with the isolines of the density field (Döös and Webb, 1994; Viebahn and Eden, 2012). The time-mean of the isopycnal stream function is given by

$$\overline{\psi_I}(\theta, \sigma) = \overline{\oint_0^{2\pi} \int_{\eta_B(\phi,\theta)}^{\eta(\phi,\theta,t)} v(\phi, \theta, z, t)\, \mathrm{d}z\, R\cos(\theta)\, \mathrm{d}\phi} \tag{3}$$

where ϕ, θ and z are the usual spherical coordinates, R is Earth's radius and σ is potential density. η_B is the depth of the ocean bottom and $\eta(\phi, \theta, t)$ is the depth of the surface of constant σ that varies in both space and time. $\overline{(\cdot)}$ denotes the averaging operator with respect to the time coordinate.

The overturning streamfunction is split into various components by decomposing the velocity and density fields into different terms that each are governed by distinct physics. The decomposition here consists of separating the velocity and density field into a time-mean and the deviation about it, $v(\phi, \theta, z, t) = \overline{v}(\phi, \theta, z) + v^*(\phi, \theta, z, t)$, and likewise for σ. The isopycnal streamfunction that arises from the time-mean fields is here denoted Ψ_I and is given by

$$\Psi_I(\theta, \overline{\sigma}) = \oint_0^{2\pi} \int_{\eta_B(\phi,\theta)}^{\overline{\eta}(\phi,\theta)} \overline{v}(\phi, \theta, z)\, \mathrm{d}z\, R\cos(\theta)\, \mathrm{d}\phi, \tag{4}$$

where $\overline{\eta}$ is the height of the time-mean density surface $\overline{\sigma}$. The difference between the time-mean of the isopycnal streamfunction and the streamfunction derived from the time-mean fields is the deviation from the time-mean,

$$\psi_I^* = \overline{\psi_I} - \Psi_I, \tag{5}$$

which captures the motion that varies on a temporal time scale shorter than the time span of the applied time-averaging operator. On a time scale less than a couple of months, the transient mesoscale eddy field is known to be a dominating contribution to ψ_I^* (Ballarotta et al., 2013), and its nature is to oppose the time-mean flow. The residual that arises from the cancellation between these two cells is thus given by the isopycnal streamfunction $\overline{\psi_I}$, which advects tracers and other physical properties.

The mesoscale eddy field is not resolved in the coarse resolution 1° model and is instead represented by the eddy-induced transport velocities given by the implemented eddy parameterization. The isopycnal overturning streamfunction is here calculated as

$$\begin{aligned}\overline{\psi_I} \;=\; & \overline{\oint_0^{2\pi} \int_{\eta_B}^{\eta} v\, \mathrm{d}z\, R\cos(\theta)\, \mathrm{d}\phi} \\ & + \overline{\oint_0^{2\pi} \int_{\eta_B}^{\eta} v_{\mathrm{GM}}\, \mathrm{d}z\, R\cos(\theta)\, \mathrm{d}\phi}\end{aligned} \tag{6}$$

where v_{GM} is the meridional component of the eddy-induced velocity field. The first term on the right hand side of eq. (6) is the overturning streamfunction associated with the mean-flow and the second term is the time-mean eddy-induced overturning streamfunction, which in the analysis that follows are compared to the high-resolution overturning streamfunctions Ψ_I and ψ_I^*, respectively.

3.1. Choice of temporal resolution

As seen from satellite altimetry, Frenger et al. (2015) reports that the mean lifespan of a Southern Ocean eddy is about ten weeks. This is supported by the study by Ballarotta et al. (2013), who uses a 1/4° global ocean model to show that an estimate of the overturning streamfunction obtained with the use of monthly-mean output fields captures the majority of the eddy variability. However, the present study uses a model of 1/10° resolution which possesses more energy at the high frequencies and large wavenumbers. To assess the difference in the representation of the residual meridional overturning circulation in the 1/10° model at different temporal resolution, we compute $\overline{\psi_I}$ of Htau05 with both monthly-mean and three-day mean model output.

The left panel of Fig. 3 shows the ten-year mean of ψ_I^* between model year 33 and 42, calculated using monthly-mean fields. The right panel shows the same as the left panel, but calculated using three-day mean output. The characteristics of the eddy-induced overturning is discussed in the succeeding section, and here we focus on its dependence on temporal resolution only. The structure of ψ_I^* is more or less independent from the temporal resolution of the output fields, but its magnitude does vary. The minimum in the heavier water masses changes from − 10Sv to − 14Sv when the temporal resolution is increased, but the second minimum closer to the surface between 50°S and 40°S changes by less than 1 Sv. The latter minimum is associated with the overturning in the upper cell, which has been the primary focus in the discussion of eddy compensation in the Southern Ocean.

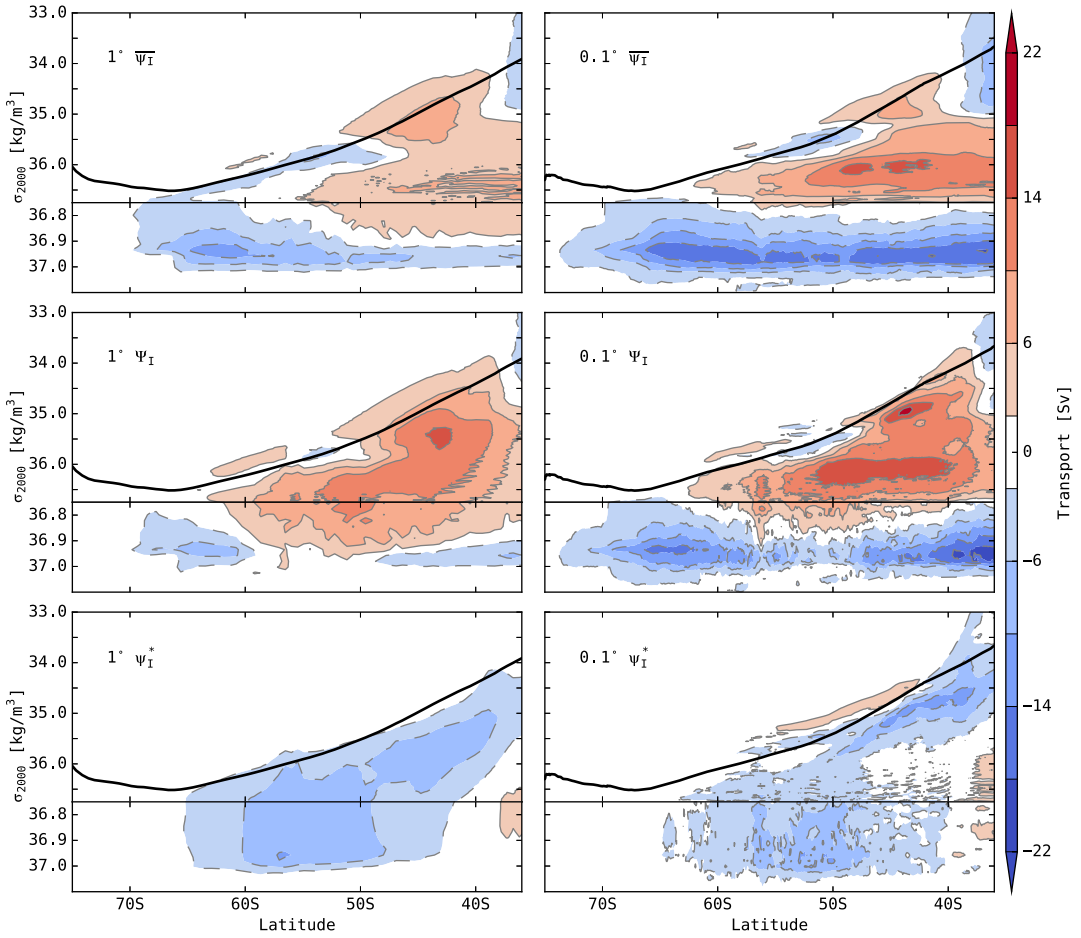

Fig. 4. The Figure displays the residual overturning $\overline{\psi_I}$ (upper row), the overturning of the time-mean flow Ψ_I (middle row) and the bolus overturning ψ_I^* (lower row) for the control integration of the 1° model (left column) and the 0.1° model (right column). The overturning from the 1° model is the mean from year 290 to 299, whereas the overturning from the 0.1° model is based on a mean from year 16 to 25. The transient eddy overturning ψ_I^* is computed directly from the parameterized bolus velocities in the coarse resolution model. In the high resolution model, this overturning is obtained by subtracting Ψ_I from $\overline{\psi_I}$. Units are in Sv, 1 Sv $\equiv 1 \times 10^6$ m^3/s, and color interval is 4 Sv. The black solid line is the zonal mean of the time-mean surface potential density field, and provides an approximate measure of the surface ocean. Note the non-linear y-axis.

Since this eddy motion appears to vary mostly on a time scale that exceeds a month, an appropriate estimate of the overturning metrics is possible to obtain by using monthly-mean fields. The minimum of the eddy overturning in the densest water is though underestimated by approximately 30% by this choice. The results presented in the subsequent section are all computed using monthly-mean fields since the main focus of this study is on the upper overturning cell.

4. Results

4.1. Background state overturning

Fig. 4 presents the ten-year mean spatial structure of the meridional overturning circulation in the Southern Ocean from the two default simulations, as well as its decomposition, as function of potential density referenced to 2000 db. The decomposition of the overturning follows the procedure outlined in Section 3 and the potential density axis was discretized into 200 equally-spaced levels between 1033.0 kg/m^3 and 1037.5 kg/m^3 for both model solutions. The black solid line in all panels is the zonal mean of the surface potential density field averaged over the same ten-year time span, and gives an approximate indication of the ocean surface.

The residual circulation (upper panels, Fig. 4) from both models in general show a quasi-adiabatic inflow of circumpolar deep water to the Southern Ocean in the density range 1036.5 kg/m^3–1037.0 kg/m^3 and a transformation and separation of water masses as the water upwells at higher southern latitudes. The water that upwells north of the separation point gains buoyancy at the surface and returns northward in the surface Ekman layer. This flow pattern is referred to as the upper cell (Farneti et al., 2015). Transformation of lower circumpolar deep water, the denser fraction of the water that enters the Southern Ocean, to bottom water between 65°S and 75°S is also seen in both model solutions, which replenish the bottom water masses that partly flows northward in the abyss and partly upwells due to mixing (Marshall and Speer, 2012). This circulation is referred to as the lower cell. Other cells, such as the anti-clockwise subtropical cell and anti-clockwise recirculation between 50°S and 55°S, are also seen at both model resolutions, but are not discussed further (see Farneti et al. (2015) for a thorough discussion on these cells).

The amount of dense water that flows into the Southern Ocean at 40°S, and subsequently upwells, is about 30 Sv in Hcont, but only ~ 12 Sv in Ccont. From the minimum and maximum of the lower- and upper cell, respectively, it is seen that the water that upwells to the surface divides approximately evenly between the two in Hcont, with an overturning of 15 Sv in the upper cell and 17 Sv in the lower cell. In Ccont, a substantial recirculation is seen in the lower cell, with a bottom water formation of 12 Sv between 70° and 60°S, but only 5 Sv leaves the domain to the north through the abyss. This is an expression of the weak formation of Antarctic Bottom Water in Ccont (Gent et al., 2011). The remaining 7 Sv that enters the Southern Ocean leaves through the upper cell. Similar residual overturning structures are also seen in the coupled model configuration of CESM, as well as the difference between

the high and the low resolution runs, albeit with overall stronger amplitude due to overly strong modelled Southern Ocean winds (Gent and Danabasoglu, 2011; Bishop et al., 2016). In comparison to the multi-model study by Farneti et al. (2015), the upper cell strength of 7 Sv in Ccont is considerably weaker than the 12 to 18 Sv found in most state-of-the-art coarse resolution climate models forced with the CORE.v2 1958 – 2007 reanalysis product. This difference is at least partly explained by the fact that the Southern Ocean winds are subject to a ~ 30% intensification in this period.

The time series of the maximum and minimum of the upper and lower cell of the residual meridional overturning circulation from Hcont (upper right panel of Fig. 4) are shown by the black and green curve in Fig. 5, respectively. Both time series show pronounced inter-annual variability that arises from the resolved eddy field, and an annual cycle is also visible. The maxima of the upper cell fall during the austral winter months where the zonal winds and the northward surface Ekman current are the strongest (See Yuan, 2004, for an observational estimate of the seasonality in the Southern Ocean winds). The minima of the bottom cell also occur during the winter months and is associated with the production of dense water due to an intense buoyancy loss to the atmosphere and brine rejection from sea ice formation. Also, neither time series possess any clear trend although the first two years of the lower cell appear to have a stronger (more negative) summer overturning. The same time series are also provided for Ccont (magenta and blue lines for the upper and lower cell, respectively) which are seen to share many features with Hcont, but with a more uniform annual cycle and a weaker circulation in general that was also reflected in the spatial structure of the residual overturning (upper panels, Fig. 4).

Looking into the decomposition of the meridional flow, the overturning that arises from the time-mean velocity fields (middle panels, Fig. 4) is overall stronger than the residual, and the subsurface maximum of the upper cell is also more comparable between the two models. This is not a surprise as the models are subject to identical surface boundary conditions and no cancellation from the transient eddies is present in this metric. A closed cell of clockwise circulation is also seen in both model solutions at the surface at about 1035 kg/m^3 and 45°S, again present in the coupled model solutions as well. It is also interesting to note that the flow in the abyss between 60°S and 50°S is entirely eddy-induced in Ccont (left panel), but only partly at 0.1° resolution (right panel).

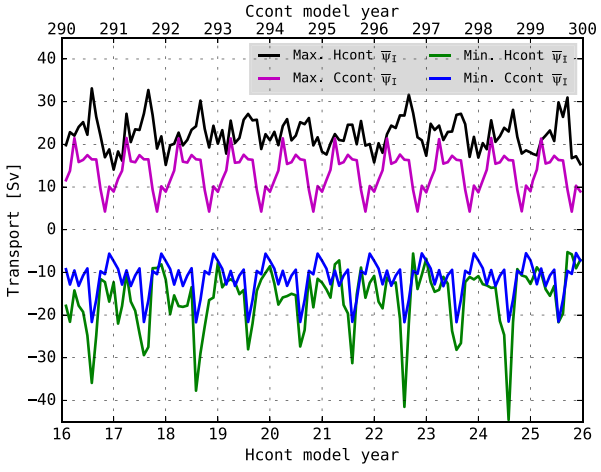

Fig. 5. Time series of the Southern Ocean meridional overturning strength from the Ccont and Hcont experiments based on monthly means. The maximum streamfunction (black and magenta line for Hcont and Ccont respectively) reflects the subsurface strength of the upper cell and is extracted from south of 40°S. The minimum streamfunction (green and blue line for Hcont and Ccont respectively) is the strength of the lower cell at 60°S. All time series reflect circulation of water denser than 1035.7 kg/m^3. The upper and lower x-axis belong to the Ccont and Hcont time series, respectively. Units are in Sverdrups. (For interpretation of the references to colour in this figure legend, the reader is referred to the web version of this article.)

The flow driven by the transient eddies is different between the two models (lower panels, Fig. 4). Whereas both models show that the eddy cell in general counteracts the time-mean flow and that the cells span the same latitude-density space, the minima of the eddy-driven overturning is differently located. The parameterized eddy field gives rise to a subsurface minimum in the densest waters between 50°S and 60°S and another subsurface minimum around 45°S and 1035.75 kg/m^3 (left panel). The explicit eddy field (right panel) also gives rise to the subsurface minimum in the densest water, but has a vanishing subsurface flow around 1036 kg/m^3 between 40°S and 50°S. This difference in spatial structure gives rise to different cancellations between the time-mean and the eddy-induced flow, resulting in the weaker residual overturning of the upper cell in the coarse resolution model.

4.2. Wind stress perturbation experiments

4.2.1. Circulation response

The model response that follows from the wind stress perturbations is reflected in the residual meridional overturning circulation, shown in Fig. 6. The panels display the difference between the perturbation experiments and the control, in accord with the averaging intervals mentioned in Section 2. The upper row of panels display the results from the high resolution model and the middle row of panels from the coarse resolution model. The left, middle and right column of panels is for the tau05, tau15, and tau20 experiment, respectively.

In terms of structure and absolute magnitude, Ctau05 and Htau05 show similar transient responses to the wind stress decrease. Both models show a weakening of similar magnitude of the upper overturning cell, and a smaller weakening of the lower overturning cell confined to high southern latitudes. The maximum of the upper overturning cell in Htau05 decreases from 15 Sv to 6 Sv, a 60% reduction, whereas the upper cell of Ctau05 collapses and finds a decrease of the upper cell maximum by 9 Sv, which corresponds to 130% relative decrease. The weakening of the lower cell corresponds to a northward retreat in both models, and the cell strength changes from 10 Sv to 6 Sv in Ctau05, and from 17 Sv to 10 Sv in Htau05, at 65°S. The ten-year mean Drake Passage transport decreases in Ctau05 and Htau05 by 12 and 4 Sv with respect to their control values, respectively (see Table 2), during the same time interval.

Shifting focus to the wind stress increase experiment, it is immediately seen that Ctau15 and Htau15 are subject to different transient model responses. Ctau15 finds a general increase of the upper cell and an increase, and displacement, of the maximum from 7 Sv to 14 Sv, as well as an increase in the zonal transport by 11 Sv. A greater value of the average thickness diffusivity, κ, is also seen (Table 2), but the change amounts to less than 10% compared to Ccont. Relatively small changes are seen in the lower cell between 70°S and 60°S, but a closer inspection also reveals that the positive changes seen in the densest waters between 60°S and the northern Southern Ocean reflects a weakening of the northward movement of bottom water. Suprisingly Htau15 shows a weakening of the upper cell and a relatively large increase in the Drake Passage transport by 47 Sv, opposite to the response seen in Ctau15 and different from the structure of the weakening seen in Htau05. The maximum of the upper cell decreases by about 3 Sv, but the lower cell increases in strength by several times the control value, fundamentally different to Ctau15. The inflow of water to the Southern Ocean increases in the 0.1° model, but the vast majority of the water enters the lower cell and leaves the domain through the abyss. The water that inflows in the 1° model increases as well, albeit weakly, but this water leaves the domain entirely through the upper cell.

The root cause of the different circulation responses to the stronger winds is at least partly due to the onset of deep convection in the Weddell Sea in Htau15. This response is similar to the model simulation presented in Cheon et al. (2013) in some aspects, and causes a sea ice retreat and an anomalous heat loss from the ocean to the atmosphere. A

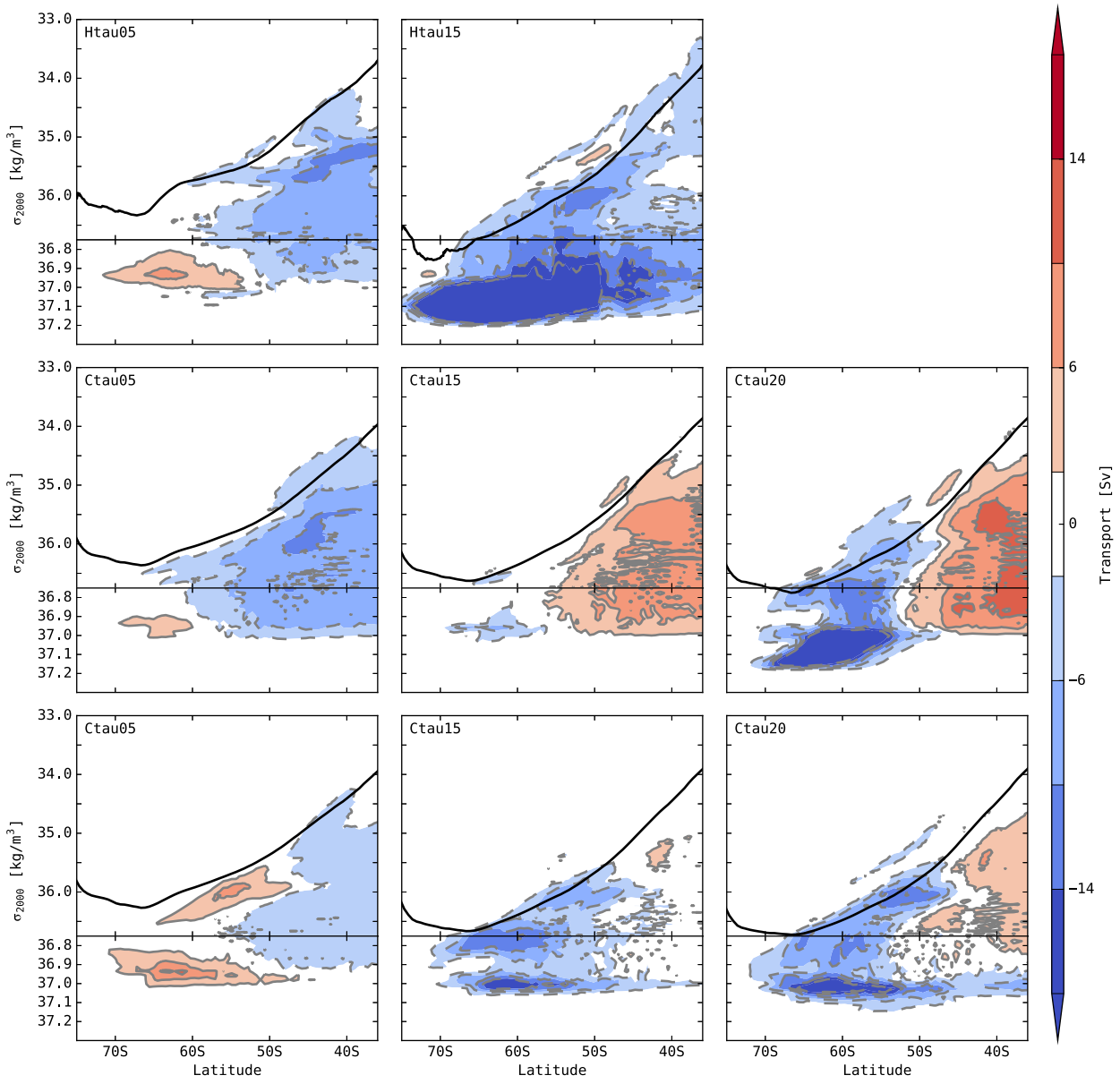

Fig. 6. The figure shows the difference in ten-year mean estimates of $\overline{\psi_I}$ between the wind stress perturbation experiments and the control simulation. The left, middle and right column of panels show the difference for the tau05, tau15 and tau20 experiment. The upper and middle row of panels are with respect to the high resolution model and the coarse resolution model, respectively. The averaging intervals are outlined in Section 2. The lower row of panels is also from the coarse resolution model, but display the difference in $\overline{\psi_I}$ on centennial time scale (average is taken between model year 390 and 399). Note the non-linear y-axis.

Table 2
Drake Passage volume transport T_{DP} and effective thickness diffusivity κ. The thickness diffusivity metric is computed as in Jochum and Eden (2015), and consists of a vertical average between 200 m and 1000 m depth, a meridional average between 66°S and 38°S, and a complete zonal average. All measures are ten-year means, and are computed within the time spans outlined in Section 2. The Ccont value of κ is 521 m^2/s.

Exp.	κ [m^2/s]	T_{DP} [Sv]
Htau05	N/A	129
Htau15	N/A	180
Ctau05	521	124
Ctau15	561	147
Ctau20	690	196

detailed account of the physical processes that lead to a destabilization of the water column is beyond the scope of the present study. It is though relevant to remark that minor differences in the Weddell Sea background stratification between Ccont and Hcont prevents deep convection in Ctau15 (the Weddell Sea hydrography is in general sensitive to model setup, see e.g. Kjellsson et al. (2015)). A stronger increase in the zonal wind stress in the coarse resolution model by 100% (Ctau20) does trigger Weddell Sea deep convection and enhances the lower overturning cell in a similar manner as seen in Htau15 (Fig. 6, right middle panel), but the upper overturning cell appears less affected. Also, as seen from Table 2, both κ and the Drake Passage transport enhance by 32% and 44%, respectively, which indicate substantial changes in the ocean stratification.

The difference in involved physics in principle render a comparison of the eddy compensation between Ctau15 and Htau15 inappropriate, because the eddy-induced overturning component ψ_I^* of Htau15 is influenced by the transients of the bottom water formation. This difference in the behavior of the residual meridional overturning circulation in Ctau15, Htau15 and Ctau20 displays that the Southern Ocean model response is far from trivial when two overturning cells are present, as is

the case in more comprehensive ocean models.

As previously emphasized in the literature (e.g. Munday et al., 2013), eddy compensation is a steady-state argument. The lower left and middle panel of Fig. 6 display the difference in the ten-year mean residual overturning from Ctau05 and Ctau15 after 100 years worth of model integration and thus closer to model equilibrium. On centennial time-scale, both experiments unequivocally show that the initial response in the upper cell attenuates and that the transport anomaly in the lower cell grows. Ctau05 now features a more modest decrease in the upper cell maximum of 4 Sv, corresponding to a 43% reduction, and Ctau15 has regained its control value of approximately 7 Sv. Consistently, Ctau20 (lower right panel) also shows a weakening of the initial upper cell response with time. From the perspective of parameterized eddies, this comparison indicates that the adjustment time of the Southern Ocean overturning takes place on centennial time scale, possibly beyond, and that the bottom route as an outflow from the Southern Ocean appears to grow in importance as the overturning system equilibrates. This calls into question whether eddy compensation is meaningfully inferred from the residual meridional overturning as seen in complex model simulations, with a representation of both the upper and lower overturning cells and variable surface buoyancy forcing, that has not fully equilibrated.

Again comparing to the coupled model studies that similarly use CESM, Gent and Danabasoglu (2011) reports a 1.4 Sv increase of the upper cell 100 years subsequent to an increase of the zonal wind stress by 50%, and the recirculation in the lower cell is seen to increase as well (their Figure 3), but with a smaller outflow of the densest water. The present study similarly finds a weak response of the upper cell on a centennial time scale, though with a stronger outflow from the Southern Ocean in the abyss compared to Ccont. On decadal time scale, a comparison between the high resolution model responses is possible. With active deep convection Htau15 is different to its coupled model counterpart in Bishop et al. (2016) and finds a 20% weakening of the upper cell where they find a strenghening by 39%. However, both model finds a strengthening of the lower cell, which in their study is connected to a thinner austral winter sea ice cover in the Weddell Sea (see their Figure 13), much alike the physical response presented here.

4.2.2. Changes in the 1036.5 kg/m^3 density surface

The change in the meridional slope of the Southern Ocean isopycnals is a salient measure pertinent to the discussion on the response of the circulation to a wind stress change due to the prevailing thermal wind balance. In addition, this metric should not be significantly influenced by the deep convection event in regions away from the Weddell Sea which allow us to indirectly infer the degree of compensation in Htau15. The upper panels of Fig. 7 show the time-mean depth of the 1036.5 kg/m^3 potential density surface, henceforth denoted by $\sigma_{36.5}$, from Ccont (left) and Hcont (right). The remaining stereographic plots in the left column display the vertical displacement of the isopycnal between the wind stress perturbation experiments and the control integration for the coarse resolution model. The depth changes in the high resolution model is shown in the right column, and the lowermost plot shows the zonal mean difference in isopycnal depth for all experiments. The difference is taken between the ten-year means that are outlined in Section 2.

The choice to map the changes in $\sigma_{36.5}$ is motivated by Fig. 4, which show that the upwelling in the Southern Ocean associated with the upper residual overturning cell is approximately along this density surface in both models. Both Ccont and Hcont finds that $\sigma_{36.5}$ sits at a depth that exceeds 1 km in the periphery of the Southern Ocean, and that it outcrops between 50°S and 60°S. This is in agreement with the residual meridional overturning circulation, which shows that water of density 1036.5 kg/m^3 is subject to upwelling and transformation in this latitude band.

Ctau05 and Htau05 both show a response that holds a zonal pattern; a deepening of the isopycnal at high southern latitudes and a rise in the mid-latitudes. This corresponds to a weakening of the meridional slope of $\sigma_{36.5}$ and a southward displacement of the outcrop line. Regional differences do exist between the two model responses, but the large-scale structure is similar. This is also seen from the lowermost panel, which shows that the peak zonally-averaged vertical depression of $\sigma_{36.5}$ (magenta lines) is about 50 m at high southern latitudes in both Ctau05 and Htau05.

True to both models, $\sigma_{36.5}$ rises at high southern latitudes, equivalent to a steepening, and is depressed farther to the north for the 50% wind stress increase. The rise of $\sigma_{36.5}$ in Ctau15 is rather modest and mirrors the response seen in Ctau05 to a high degree, which is also visible in the zonal mean (solid blue line). The high resolution model, on the other hand, has an increase of the isopycnal tilt of greater magnitude. The greater rise along the path of the Antarctic Circumpolar Current is expected to be the outcome of a complex interplay between the active deep convection in the Antarctic polar seas, the stronger winds and the transient eddy response. However, the deepening in the northern part of the domain takes place relatively far away from the deep convection zones and the response is therefore expected to follow the Ekman and eddy dynamics alone. Despite the two local maxima in the deepening in the Atlantic sector of Htau15, Ctau15 overall finds the strongest response in the northern part of the Southern Ocean. As seen from the zonal mean (blue lines), $\sigma_{36.5}$ displaces with $\sim$ 50 m in Ctau15 whereas Htau15 finds a zonally-averaged maximum deepening of about 25 m. This suggests a stronger parameterized sensitivity in Ctau15 to the zonal wind stress increase compared to Hcont15.

4.2.3. Northward heat transport response

To enable a direct comparison between Bitz and Polvani (2012), Bryan et al. (2014) and the present study, we investigate the total northward heat transport and its decomposition into contributions from the mean-flow and the eddy-induced circulation. The upper panel of Fig. 8 shows the total northward heat transport, the middle panel the transport by the mean flow and the lower panel the eddy heat transport. The heat transport estimate from the coarse resolution model (solid lines) includes both the heat advection by the bolus velocities and isopycnal diffusion of heat, and the contribution from submesoscale eddies is not included. The total northward heat transport in the high resolution model (dashed lines) is obtained by integrating $\overline{v\theta}$ in the zonal and the vertical, and the eddy component is obtained by subtracting the product $\overline{v}\,\overline{\theta}$ from $\overline{v\theta}$ (here θ denotes potential temperature). Horizontal diffusion of heat due to the biharmonic operator is orders of magnitude smaller than the advective terms and is therefore not included.

The total heat transport of Ccont and Hcont (solid and dashed black lines, upper panel) both show that it is directed southward everywhere in the Southern Ocean, and that the two models deviate the greatest between 60°S and 50°S with about 0.1 PW. The estimates are in agreement with those modelled by Bryan et al. (2014, their Fig. 2), but with a less strong discrepancy north of 40°S. The decomposition shows that the northward heat transport by the mean flow (middle panel) is overall weaker in Hcont. The eddy contribution (lower panel) is southward at all latitudes in both models, but the parameterized eddies suggest a greater southward eddy heat transport than Hcont, as was also the case in Bryan et al. (2014).

Ctau05 and Htau05 (magenta lines) agree that the northward heat transport decreases north of 55°S when the wind stress is reduced. This is primarily due to the changes in the mean flow, which follow from the reduced northward surface Ekman drift, as was also seen in the residual overturning response shown in Fig. 6. This change is partly balanced by a reduced southward heat transport by the eddies. Ctau05 suggests a stronger weakening in the total northward heat transport, which is a result of a greater change in the mean flow heat transport compared to Htau05, in concert with a weaker parameterized eddy response.

As was already seen from the response in the residual overturning circulation and the density structure, Ctau15 and Htau15 (blue lines)

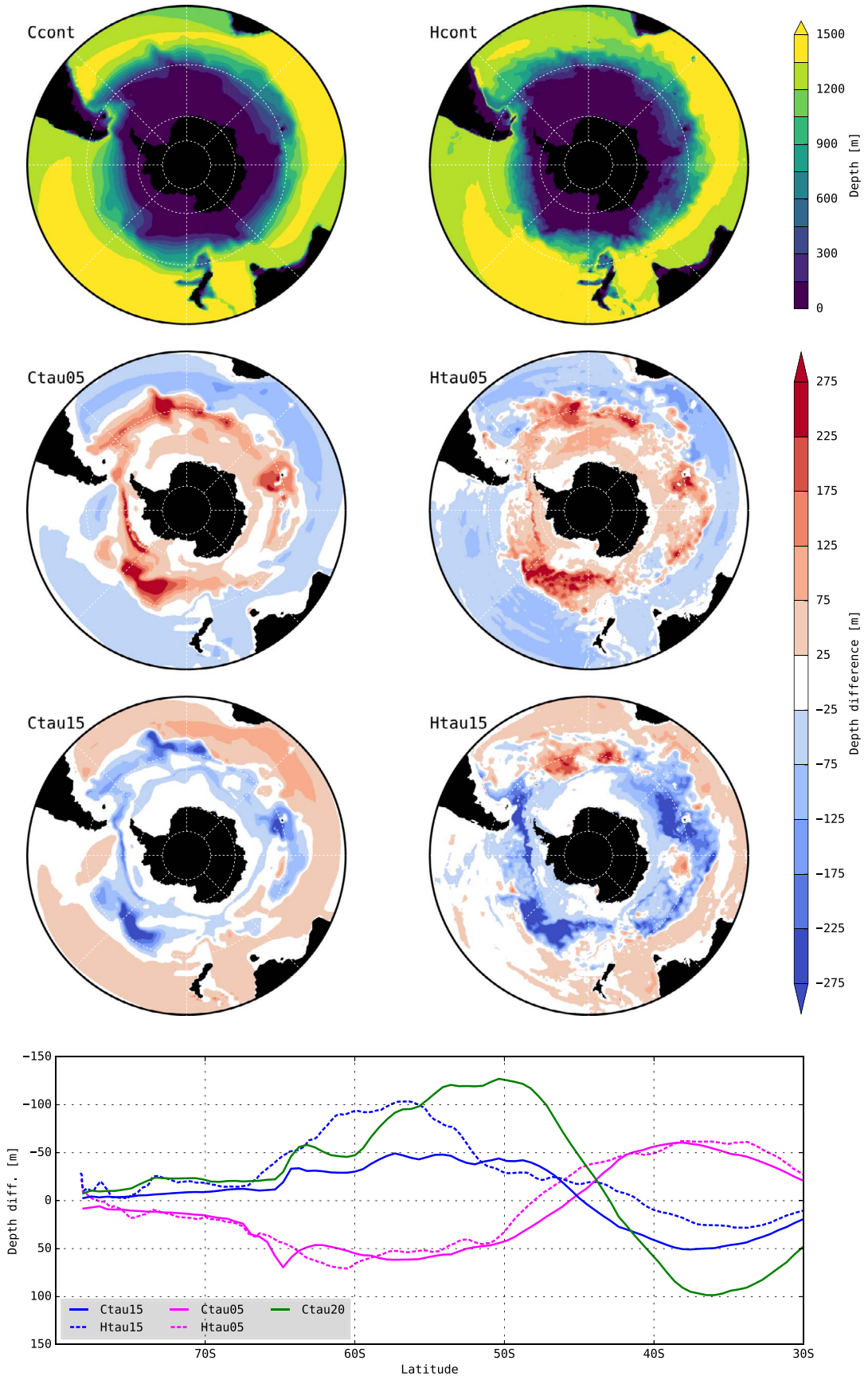

Fig. 7. The panels display the depth and vertical displacement of the 1036.5 kg/m^3 isopycnal estimated from the time-mean potential density field referenced to 2000 db. The left and right column of plots is associated with the coarse and high resolution model, respectively. The upper row display the ten year mean depth of the isopycnal from Ccont and Hcont. The second and third row show the difference between the perturbation experiment and control for tau05 and tau15. The time-averaging intervals are stated in Section 2. The units are in meters. The lower panel displays the zonally-averaged depth difference as function of latitude.

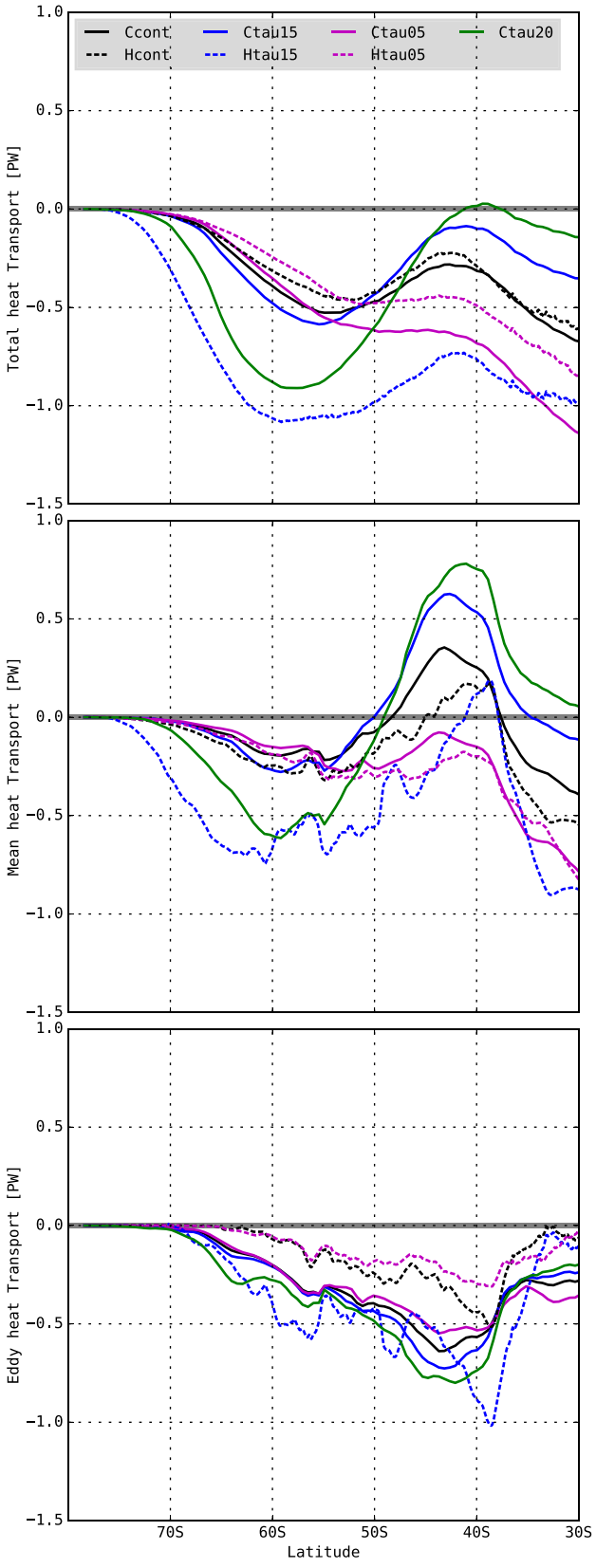

Fig. 8. The upper panel displays the total northward heat transport for tau05 (magenta), cont (black), tau15 (blue) and tau20 (green). The middle and lower panel show the heat transport contributions from the mean-flow and from the eddy-induced flow, respectively. The results from the coarse resolution model are shown in solid lines and the high resolution model with dashed lines. (For interpretation of the references to colour in this figure legend, the reader is referred to the web version of this article.)

respond differently to the 50% wind stress increase. Ctau15 shows a response that is opposite to that seen in Ctau05 in the total heat transport and its two components. Htau15, on the other hand, shows that the total heat transport becomes increasingly southward everywhere, with a peak southward transport beyond 1PW around 60°S. Recalling that the eddy transport also encompasses the transient response from the convection in the Weddell Sea, the decomposition shows that both the mean flow and the eddy transport contributes to the increased southward heat transport. As was evident from Fig. 6, the Htau15 circulation intensifies as function of the stronger winds, but the majority of the water densifies upon upwelling and enters the lower overturning cell. Fig. 8 shows that this enhanced poleward flow also increases the amount of heat that is transported southward. A similar response is also seen in Ctau20 (green lines) where the southward heat transport is increased south of 50°S, mainly due to the changes in the mean-flow. The heat transport in the northern part of the Southern Ocean does not appear to be affected the same way as Htau15 by the convection in the polar seas. This is in line with the residual overturning response, seen in the middle right panel of Fig. 6, where both the upper and lower cell strength of Ctau20 increases as function of the stronger wind stress.

4.2.4. *Buoyancy forcing response*

An increase in the residual meridional overturning circulation must be accompanied with an increase in the transformation of water masses in the ocean mixed layer. We therefore examine the surface buoyancy forcing changes to the wind stress perturbations to understand the thermodynamical response associated with the changes in $\overline{\psi_l}$. We adopt the same approach as in Bishop et al. (2016) and compute the ocean surface buoyancy forcing as function of the surface heat fluxes, atmospheric fresh water contributions from precipitation and evaporation, prescribed river run-off and contributions from interactions with the active sea ice model. The upper panels of Fig. 9 show the Ccont (left) and Hcont (right) ten-year mean surface buoyancy forcing fields. A positive buoyancy forcing indicates that the ocean surface became fresher and/or warmer. It is seen that the forcing field of Ccont and Hcont holds a similar structure; in the long term mean, the ocean surface losses buoyancy along the coast of Antarctica due to brine rejection, gains buoyancy below the sea ice due to ice melt (Abernathey et al., 2016), and warm western boundary currents release heat to the relatively colder atmosphere above. The largest difference between Ccont and Hcont is seen in the Indian sector, where a strong meridional gradient associated with the Antarctic Circumpolar Current is present in Hcont, but not in Ccont.

The zonally-averaged difference in surface buoyancy forcing between the wind stress change experiments and the control simulations is seen in the lower panel of Fig. 9. Changes in the buoyancy forcing reflect changes in ocean surface properties and sea ice cover since the meteorological forcing fields are prescribed. The coarse resolution model reponse to the 50% wind stress increase and decrease is approximately linear, as was also the case in the changes of $\overline{\psi_l}$ and $\sigma_{36.5}$, and the modelled response is confined to north of 60°S. This latitude coincides approximately with the austral winter sea ice edge (Fig. 1). Ctau15 (blue solid line) gains more buoyancy in the region where water upwells, consistent with an equatorward displacement of the $\sigma_{36.5}$ outcrop latitude (Fig. 7), and an increased residual overturning circulation in the upper cell (Fig. 6). Vice versa, Ctau05 (solid magenta line) finds a decrease in the buoyancy forcing in accord with a relaxation of the isopycnal slope and decrease in the upper cell strength. The Htau05 buoyancy forcing response (dashed magenta line) is in many ways similar to Ctau05, although it suggests a buoyancy gain about 40°S relative to Hcont.

The changes in the buoyancy forcing in the model simulations that involve enhanced deep convection, Htau15 and Ctau20, behaves differently compared to Ctau15. Htau15 (blue dashed line) finds a zonally-averaged buoyancy loss throughout the Southern Ocean, most notably

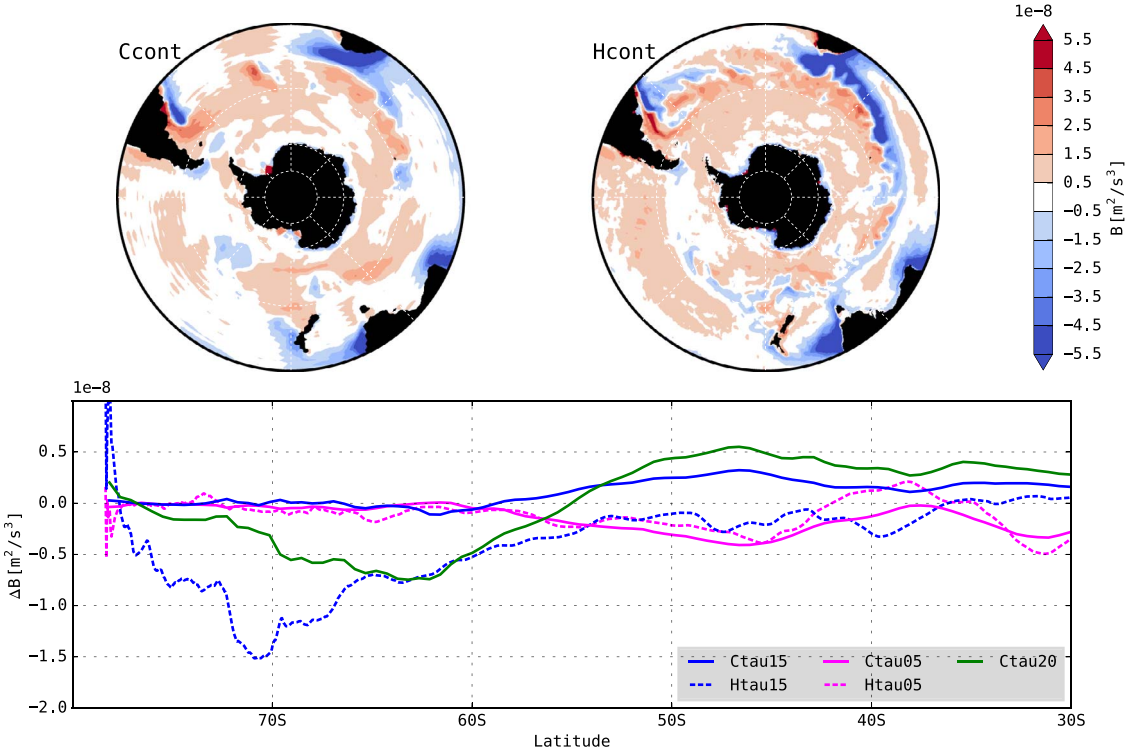

Fig. 9. The upper left and upper right panel shows the ten-year mean buoyancy forcing in Ccont (left) and Hcont (right). The color interval is 1×10^{-8} m^2/s^3. A positive buoyancy forcing implies that the ocean surface became fresher and/or warmer. The lower panel shows the zonally-averaged difference in ten-year mean buoyancy forcing between the wind stress perturbation experiments and the control integrations.

at 70°S where the response peaks at -1.5×10^{-8} m^2/s^3. This is the expression of a strong heat loss to the atmosphere due to a reduced sea ice cover in this model simulation. This is also the region where bottom waters are formed in Hcont (Fig. 4), and explains the much stronger lower cell seen in Fig. 6. Accordingly, Ctau20 (green solid line) also finds a strong heat loss at high southern latitudes and a stronger lower cell. The upper cell does not strengthen in Htau15 despite the stronger winds, and the buoyancy forcing response suggests that the reason is a thermodynamical constraint on the water mass transformation. This constraint is not present in Ctau20, where the mid-latitudes gains more buoyancy than in Ccont, why the upper residual overturning cell increases as function of the stronger winds.

5. Discussion

The decomposition of the residual meridional overturning circulation seen in Fig. 4 shows that the lower cell in the control simulations is weaker in Ccont compared to Hcont. This is largely explained by differences in the mean-flow circulation (middle panels, Fig. 4). In addition to the fact that it is overall weaker, it is also more or less absent between 60°S and 50°S and does not extend as far southward as seen in Hcont. This mismatch between the two simulations is most likely a function of the inability of the coarse resolution model to produce dense bottom waters, which is a common shortcoming of most CMIP5 models (Heuzé et al., 2013). In support of this conclusion, the buoyancy forcing fields from Ccont and Hcont (Fig. 9) also shows that the Antarctic coastal buoyancy loss is greater in Hcont and therefore allows for a greater dense water formation.

The upper mean-flow overturning cell has a closer resemblance between the two models and the dissimilarity in the residual of the upper cell is primarily a function of the eddy-induced flow, which in the lower panels of Fig. 4 is shown to have a different structure in latitude-density space. Specifically, the flow of water between 50°S and 40°S with densities about 1036 kg/m^3 is poorly represented in Ccont as Hcont suggests a more surface-intensified eddy-driven circulation. More promising is the parameterized eddy-flow in the most dense water between 60°S and 50°S which compares better to Hcont. As seen from Fig. 3, this part of the eddy circulation in Hcont is however underestimated in ψ_I^* by our choice of using monthly-mean output in the computation of $\overline{\psi_I}$. This is not the case with respect to the discrepancy in the upper cell, which is not an artifact of a misrepresentation of ψ_I^*, but rather originates in the limitations of the Gent–McWilliams parameterization. Differences in the surface buoyancy forcing are able to contribute to the difference in the residual overturning circulation as well. This effect is though ascribed a minor contribution given that the Ccont and Hcont forcing fields are similar in both structure and magnitude, as seen from Fig. 9.

A similar result was found in the inter-model comparison study by Farneti et al. (2015). They estimated the eddy-induced overturning circulations that arise explicitly in the GFDL and Kiel ocean models of 1/4° horizontal resolution and compared it to the circulation from the coarse resolution version of the same models. Admittedly not able to resolve the full eddy field, especially not at high southern latitudes, the eddy permitting models do indicate that the parameterization either do not represent or significantly underestimates the eddy-induced flow in the lighter water masses close to the surface to the north of 50°S (see their Figure 18), which is the case in the present study as well. That a discrepancy between the resolved and parameterized eddy-induced overturning circulation exists is perhaps not unexpected. For example, it has previously been shown that a down-gradient closure for eddy fluxes of isopycnal thickness is of limited skill (Roberts and Marshall, 2000), and that ambiguity remains to the optimal choice of the thickness diffusivity (Eden et al., 2009).

The parameterized sensitivity of the circulation to the Southern Ocean zonal wind stress compares well to that of an eddy-resolving model for a wind stress reduction. On decadal time scale, Ctau05 and Htau05 find a reduction of the upper residual overturning cell of comparable magnitude and spatial structure (Fig. 6). This contrasts

with Hallberg and Gnanadesikan (2006) that also investigate the overturning response on a 20 year time scale, but use a constant thickness diffusivity. In addition, both model simulations suggest a reduction of the meridional slope of $\sigma_{36.5}$, which is seen as a depression at high southern latitudes and a lift in the mid-latitudes of about 50 m in the zonal mean (Fig. 7). The same comparison for a 50% wind stress increase is made less straightforward by the complex model response of the Htau15 experiment. As noted in the results section, it might be reasonable to assume that the changes in $\sigma_{36.5}$ in the northern part of the Southern Ocean is unaffected by the deep convection in the polar marginal seas. Here Ctau15 shows a stronger response than Htau15 (Fig. 7), which might imply that the sensitivity is higher in the coarse resolution model than in the eddy-resolving model with respect to a wind stress increase. This inference is though complicated by the fact that the buoyancy forcing change is different between Ctau15 and Htau15 as well (Fig. 9).

Comparing the modelled heat transport responses to preceeding model studies (Fig. 8), Bryan et al. (2014) finds that the parameterized eddy heat transport becomes increasingly southward between 60°S and 50°S due to stronger winds in a coupled model experiment. Moreover, they find that an eddy-resolving model obtains an eddy response of opposite sign in an identical forcing scenario. In the wind stress reduction experiments analyzed in this study, the parameterized and resolved eddy field both result in a consistent weakening of the southward heat transport, and the largest response is found between 40°S and 50°S. Also, where Bitz and Polvani (2012) show that the parameterized response is stronger than the response by the explicit eddies in an ozone forcing experiment, we here demonstrate the opposite case with prescribed atmospheric forcing. This latter point is also true for the 50% wind stress increase experiments, where the explicit eddies respond strongest, even in the northern part of the domain away from the Antarctic convective zones. This inconsistency with past studies is likely the result of differences in experimental setup and the presence of ocean-atmosphere feedbacks in the coupled simulations.

The disparate transient overturning responses simulated in the Ctau15 and Htau15 experiments, displayed in the middle column of panels in Fig. 6, also deserve more attention. Despite ambiguity in terms of adjustment time and amplitude, the response seen in the Ctau15 experiment in general aligns itself with previous coarse resolution eddy-parameterizing general circulation model studies that show that the upper residual cell increases in strength as function of stronger zonal wind stress (Gent and Danabasoglu, 2011; Farneti et al., 2015). The message from high resolution model studies has been that a similar, though attenuated response is found when the eddies are explicitly resolved (Hallberg and Gnanadesikan, 2006; Munday et al., 2013). The weakening of the upper cell as seen from the Htau15 experiment contrasts with these studies, and appears to be controlled by the active deep convection in the Weddell Sea to some extent. The sea ice retreat that follows allows for an efficient loss of buoyancy that drives an enhanced formation of bottom water and an amplification of the lower cell (Fig. 9), much alike the results from the buoyancy forcing experiments presented in Jansen and Nadeau (2016).

A recent study by Hogg et al. (2017) finds a similar decrease of the upper residual cell strength in a global 1/4° resolution general circulation model in an experiment where the Southern Ocean winds are subject to a poleward shift and intensification. In accord with the present study, their overturning response is concurrent with deep convection in the Weddell Sea. Evidently compensation of the wind-driven Southern Ocean upwelling is not only possible to achieve through increased eddy activity, but also through high-latitude deep convection, which complicates an assessment of the eddy-effect in isolation from non-equilibrated model runs. Whether this result has implications for past wind stress change experiments with relatively short adjustment time and changes in surface buoyancy fluxes is not clear. The literature on Southern Ocean wind stress change experiments however shows that it is not uncommon to invoke perturbations of similar magnitude as those tested in the present study (e.g. Gent and Danabasoglu, 2011; Dufour et al., 2012; Munday et al., 2013; Jochum and Eden, 2015; Bishop et al., 2016).

Lastly we note that observations have shown that the isopycnals have subsided throughout the Southern Ocean over the last several decades as a function of stronger westerlies, but with minimal changes to the isopycnal slope (Böning et al., 2008, their Figure 4(a)). Though not directly comparable to the model responses investigated here due to the simplicity of the applied wind stress perturbations and the integration length of the experiments, it is possible to compare the nature of the modelled reponse seen in Ctau15 and Htau15 to the observations. The observations show that the modelled adjustment of the 1036.5 kg/m^3 density surface is of correct sign and is within the correct order of magnitude in the northern part of the domain, regardless of model resolution. However, neither of the models capture the deepening of $\sigma_{36.5}$ at the higher southern latitudes, and instead find an increase of the isopycnal slope and the Drake Passage transport (Table 2). The high resolution wind stress reduction experiment, Htau05, which does not experience a reduced sea ice extent, also provides evidence for a finite sensitivity of the isopycnal slope to the zonal wind stress.

Appropriate to the discussion of the results presented here is also the short spin-up of the high resolution model, and the void of a control integration through the 50% wind stress change experiments, which are obvious drawbacks to the analysis of Hcont, Htau05 and Htau15. Fig. 2 shows that the horizontally-averaged Southern Ocean temperature field drifts, and that Hcont is warmer than Ccont in the upper 1km. The time series of the overturning strength of the upper and lower cell shown in Fig. 5, as well as the Drake Passage transport time series seen in the bottom panel of Fig. 2, do provide some comfort in that the metrics under investigation do not drift prior to the initiation of the perturbation experiments. A weakening of the lower cell with time is visible (green line, Fig. 5), a result that most likely stems from an insufficient spin-up of the deep ocean, and enters the results section as an overestimation of the strength of the lower cell. The drift in Hcont also influences the results from the wind stress change experiments as the ten year means obtained from the control and the perturbation experiments are shifted in time due to the absence of a sufficiently long control integration. However, given the short integration times involved in this study and the negligible drift in the Hcont overturning strength, we do not expect remaining drift to change the results significantly.

6. Summary

We compare forced ocean general circulation model simulations of 1° and 0.1° horizontal resolution to assess the ability of the eddy mixing parameterization as formulated in Danabasoglu and Marshall (2007) to mimic resolved eddy effects. A comparison of the Southern Ocean isopycnal streamfunction from the two models shows that the coarse resolution model has a weaker transport in both overturning cells with present-day wind stress magnitude. From a decomposition of the residual overturning streamfunction into a mean-flow and an eddy-induced component, it is evident that a different distribution of the eddy circulation across water masses is responsible for a substantial part of the dissimilarity seen in the upper cell of the residual overturning. Differences in the mean-flow overturning circulation also exist, but the implication of this discrepancy is most important for the lower overturning cell. For example, the deep flow in the coarse resolution model appears to be entirely eddy-driven between 60°S and 50°S, but this is not the case in the high-resolution model. In addition, the decomposition of the meridional heat transport reveals that the parameterized poleward eddy heat flux is overly strong in the Southern Ocean.

A zonally constant decrease of the Southern Ocean zonal wind stress south of 25°S results in a decrease of similar magnitude in the upper residual overturning cell in both models. Concurrently, the meridional isopycnal slope reduces and the northward meridional heat transport

decreases, regardless of model resolution. An increase of the wind stress by 50%, on the other hand, is found to drive a complex model response in the 0.1° resolution model, but not in the coarse resolution model. On decadal time-scale, the transient response from the high-resolution model shows a weakening of the upper residual overturning cell by approx. 20% and a strengthening of the lower cell driven by enhanced bottom water formation in the Weddell Sea. This follows from a retreat of the austral winter sea ice edge that allows for a strong loss of heat to the prescribed atmosphere. In contrast, the residual meridional overturning in the coarse resolution model finds a 100% increase of the upper cell on the same time-scale, and with no discernable change in the lower cell. A 100% wind stress increase experiment with the coarse resolution model also features a reduction in Antarctic sea ice and stronger residual overturning in the bottom cell, demonstrating that the complex model response is not limited to the high resolution model.

The main conclusion from the presented suite of experiments is that the parameterized eddies are able to mimic the nature of the resolved eddy field during wind stress change, but are less skillful in representing the residual meridional overturning circulation and the heat transport for present day wind stress. In addition we also emphasize that the dynamics of eddy compensation are probably more involved than what is found in simple models (e.g. Marshall and Radko, 2003). As exemplified by the high resolution model experiment with stronger wind stress, the interaction between the sea ice and the ocean results in buoyancy forcing changes that overwhelm the eddy response. It appears that the challenge for future general circulation model studies is to design clever experimental setups that clearly isolate the effect from the eddies yet preserve the complexity of the problem.

Acknowledgements

The research leading to these results has received funding from the European Research Council under the European Community's Seventh Framework Programme (FP7/2007-2013) / ERC grant agreement 610055 as part of the ice2ice project. The authors gratefully acknowledge the Gauss Centre for Supercomputing (GCS) for providing computing time through the John von Neumann Institute for Computing (NIC) on the GCS share of the supercomputer JUQUEEN at Jülich Supercomputing Centre (JSC). The authors are also grateful for computing resources provided by the Danish Center for Climate Computing, a facility build with support of the Danish e-Infrastructure Corporation and the Niels Bohr Institute, as well as for Alison Baker (NCAR) for her help setting up CESM on JUQUEEN, and ERDA developers and maintainers Jonas Bardino and Klaus Birkelund Jensen for providing the computational infrastructure to analyze the model output. The authors also thank Carsten Eden and Laure Zanna for constructive discussions, as well as the editor and two anonymous reviewers, whose comments greatly improved the manuscript.

References

Abernathey, R.P., Cerovecki, I., Holland, P.R., Newsom, E., Mazloff, M., Talley, L.D., 2016. Water-mass transformation by sea ice in the upper branch of the Southern Ocean overturning. Nat. Geosci. 9, 596–603. http://dx.doi.org/10.1038/NGEO2749.

Ballarotta, M., Drijfhout, S., Kuhlbrodt, T., Döös, K., 2013. The residual circulation of the Southern Ocean: which spatio-temporal scales are needed? Ocean Modell. 64, 46–55. http://dx.doi.org/10.1016/j.ocemod.2013.01.005.

Bishop, S.P., Gent, P., Bryan, F.O., Thompson, A.F., Long, M.C., Abernathey, R., 2016. Southern Ocean overturning compensation in an eddy-resolving climate simulation. J. Phys. Oceanogr. 46, 1575–1592. http://dx.doi.org/10.1175/JPO-D-15-0177.1.

Bitz, C.M., Polvani, L.M., 2012. Antarctic climate response to stratospheric ozone depletion in a fine resolution oean climate model. Geophys. Res. Lett. 39, L20705. http://dx.doi.org/10.1029/2012GL053393.

Böning, C.W., Dispert, A., Visbeck, M., Rintoul, S.R., Schwarzkopf, F.U., 2008. The response of the antarctic circumpolar current to recent climate change. Nat. Geosci. 1, 864–869. http://dx.doi.org/10.1038/ngeo362.

Bronselaer, B., Zanna, L., Munday, D.R.M., Lowe, J., 2016. The influence of Southern Ocean winds on the north atlantic carbon sink. Global Biogeochem. Cycles 30, 844–858. http://dx.doi.org/10.1002/2015GB005364.

Bryan, F.O., Bachman, S., 2015. Isohaline salinity budget of the north atlantic salinity maximum. J. Phys. Oceanogr. 45, 724–736. http://dx.doi.org/10.1175/JPO-D-14-0172.1.

Bryan, F.O., Gent, P.R., Tomas, R., 2014. Can Southern Ocean eddy effects be parameterized in climate models? J. Clim. 27, 411–425. http://dx.doi.org/10.1175/JCLI-D-12-00759.1.

Chelton, D.B., DeSzoeke, R.A., Schlax, M.G., Naggar, K.E., Siwertz, N., 1998. Geographical variability of the first baroclinic rossby radius of deformation. J. Phys. Oceanogr. 28, 433–460. http://dx.doi.org/10.1175/1520-0485(1998)028<0433:GVOTFB>2.0.CO;2.

Cheon, W.G., Park, Y., Toggweiler, J.R., Lee, S., 2013. The relationship of weddell polynya and open-ocean deep convection to the southern hemisphere westerlies. J. Phys. Oceanogr. 44, 694–713. http://dx.doi.org/10.1175/JPO-D-13-0112.1.

Comiso, J. C., 2000. Bootstrap sea ice concentrations from nimbus-7 smmr and dmsp ssm/i-ssmis, version 2.Boulder, Colorado USA. NASA National Snow and Ice Data Center Distributed Active Archive Center. doi:http://dx.doi.org/10.5067/J6JQLS9EJ5HU.

Cunningham, S.A., Alderson, S.G., King, B.A., Brandon, M.A., 2003. Transport and variability of the antarctic circumpolar current in drake passage. J. Geophys. Res. 108 (C5), 8084. http://dx.doi.org/10.1029/2001JC001147.

Danabasoglu, G., Marshall, J., 2007. Effects of vertical variations of thickness diffusivity in an ocean general circulation model. Ocean Modell. 18, 122–141. http://dx.doi.org/10.1016/j.ocemod.2007.03.006.

Donohue, K.A., Tracey, K.L., Watts, D.R., Chidichimo, M.P., Chereskin, T.K., 2016. Mean antarctic circumpolar current transport measured in drake passage. Geophys. Res. Lett. 43, 11760–11767. http://dx.doi.org/10.1002/2016GL070319.

Döös, K., Webb, D.J., 1994. The deacon cell and the other meridional cells of the Southern Ocean. J. Phys. Oceanogr. 24, 429–442. http://dx.doi.org/10.1175/1520-0485(1994)024<0429:TDCATO>2.0.CO;2.

Dufour, C.O., Le Sommer, J., Zika, J.D., Gehlen, M., Orr, J.C., Mathiot, P., Barnier, B., 2012. Standing and transient eddies in the response of the Southern Ocean meridional overturning to the southern annular mode. J. Clim. 25, 6958–6974. http://dx.doi.org/10.1175/JCLI-D-11-00309.1.

Eden, C., Jochum, M., Danabasoglu, G., 2009. Effects of different closures for thickness diffusivity. Ocean Modell. 26, 47–59. http://dx.doi.org/10.1016/j.ocemod.2008.08.004.

Farneti, R., et al., 2015. An assessment of antarctic circumpolar current and Southern Ocean meridional overturning circulation during 1958–2007 in a suite of interannual core-ii simulations. Ocean Modell. 93, 84–120. http://dx.doi.org/10.1016/j.ocemod.2015.07.009.

Ferrari, R., McWilliams, J.C., Canuto, V.M., Dubovikov, M., 2008. Parameterization of eddy fluxes near oceanic boundaries. J. Clim. 21, 2770–2789. http://dx.doi.org/10.1175/2007JCLI1510.1.

Ferreira, D., Marshall, J., Heimbach, P., 2005. Estimating eddy stresses by fitting dynamics to observations using a residual-mean ocean circulation model and its adjoint. J Phys Oceanogr 35, 1891–1910. http://dx.doi.org/10.1175/JPO2785.1.

Frenger, I., Münnich, M., Gruber, N., Knutti, R., 2015. Southern Ocean eddy phenomenology. J. Geophys. Res. 120, 7413–7449. http://dx.doi.org/10.1002/2015JC011047.

Gent, P.R., Danabasoglu, G., 2011. Reponse to increasing southern hemisphere winds in ccsm4. J. Clim. 24, 4992–4998. http://dx.doi.org/10.1175/JCLI-D-10-05011.1.

Gent, P.R., Danabasoglu, G., Donner, L.J., Holland, M.M., Hunke, E.C., Jayne, S.R., Lawrence, D.M., Neale, R.B., Rasch, P.J., Vertenstein, M., Worley, P.H., Yang, Z.-L., Zhang, M., 2011. The community climate system model version 4. J. Clim. 24, 4973–4991. http://dx.doi.org/10.1175/2011JCLI4083.1.

Gent, P.R., McWilliams, J.C., 1990. Isopycnal mixing in ocean circulation models. J. Phys. Oceanogr. 20, 150–155. http://dx.doi.org/10.1175/1520-0485(1990)020<0150:IMIOCM>2.0.CO;2.

Gent, P.R., Willebrand, J., McDougall, T.J., McWilliams, J.C., 1995. Parameterizing eddy-induced tracer transports in ocean circulation models. J. Phys. Oceanogr. 25, 463–474. http://dx.doi.org/10.1175/1520-0485(1995)025<0463:PEITTI>2.0.CO;2.

Gnanadesikan, A., 1999. A simple predictive model for the structure of the oceanic pycnocline. Science 283, 2077–2079. http://dx.doi.org/10.1126/science.283.5410.2077.

Gouretski, V.V., Koltermann, K.P., 2004. Woce global hydrographic climatology: a technical report. Bundesamt für seeschifffahrt und hydrographie 35, 9pp.

Hallberg, R., Gnanadesikan, A., 2006. The role of eddies in determining the structure and response of the wind-driven southern hemisphere overturning: results from the modeling eddies in the Southern Ocean (meso) project. J. Phys. Oceanogr. 36, 2232–2252. http://dx.doi.org/10.1175/JPO2980.1.

Heuzé, C., Heywood, K.J., Stevens, D.P., Ridley, J.K., 2013. Southern Ocean water mass characteristics in cmip5 models. Geophys. Res. Lett. 40, 1409–1414. http://dx.doi.org/10.1002/grl.50287.

Hogg, A., Meredith, M.P., Chambers, D.P., Abrahamsen, E.P., Hughes, C.W., Morrison, A.K., 2015. Recent trends in the Southern Ocean eddy field. J. Geophys. Res. 120, 257–267. http://dx.doi.org/10.1002/ 2014JC010470.

Hogg, A.M., Blundell, J.R., 2006. Interdecadal variability of the Southern Ocean. J. Phys. Oceanogr. 36, 1626–1645. http://dx.doi.org/10.1175/JPO2934.1.

Hogg, A.M., Spence, P., Saenko, O.A., Downes, S.M., 2017. The energetics of Southern Ocean upwelling. J. Phys. Oceanogr. 47, 135–153. http://dx.doi.org/10.1175/JPO-D-16-0176.1.

Jansen, M.F., Nadeau, L.P., 2016. The effect of Southern Ocean surface buoyancy loss on the deep-ocean circulation and stratification. J. Phys. Oceanogr. 46, 3455–3470. http://dx.doi.org/10.1175/JPO-D-16-0084.1.

Jochum, M., Eden, C., 2015. The connection between Southern Ocean winds, atlantic meridional overturning circulation and indo-pacific upwelling. J. Clim. 28, 9250–9256. http://dx.doi.org/10.1175/JCLI-D-15-0263.1.

Johnson, G.C., Bryden, L.H., 1989. On the size of the antarctic circumpolar current. Deep-sea Res. 36, 39–55. http://dx.doi.org/10.1016/0198-0149(89)90017-4.
Kjellsson, J., Holland, P.R., Marshall, G.J., Mathiot, P., Aksenov, Y., Coward, A.C., Bacon, S., Megann, A.P., Ridley, J., 2015. Model sensitivity of the weddell and ross seas, antarctica, to vertical mixing and freshwater forcing. Ocean Modell. 94, 141–152. http://dx.doi.org/10.1016/j.ocemod.2015.08.003.
Koenig, Z., Provost, C., Ferrari, R., Sennchael, N., Rio, M.-H., 2014. Volume transport of the antarctic circumpolar current: production and validation of a 20 year long time series obtained from in situ and satellite observations. J. Geophys. Res. 119, 5407–5433. http://dx.doi.org/10.1002/2014JC009966.
Langlais, C.E., Rintoul, S.R., Zika, J.D., 2015. Sensitivity of antarctic circumpolar current transport and eddy activity to wind patterns in the Southern Ocean. J. Phys. Oceanogr. 45, 1051–1067. http://dx.doi.org/10.1175/JPO-D-14-0053.1.
Large, W.G., McWilliams, J.C., Doney, S.C., 1994. Oceanic vertical mixing: a review and a model with nonlocal boundary layer parameterization. Rev. Geophys. 32, 363–403. http://dx.doi.org/10.1029/94RG01872.
Large, W.G., Yeager, S.G., 2008. The global climatology of an interannually varying air-sea flux data set. Clim. Dyn. 33, 341–364. http://dx.doi.org/10.1007/s00382-008-0441-3.
Le Quéré, C., Rödenbeck, C., Buitenhuis, E.T., Conway, T.J., Langenfelds, R., Gomez, A., C., L., Ramonet, M., T., N., Metzl, N., Gillett, N., Heimann, M., 2007. Saturation of the Southern Ocean co2 sink due to recent climate change. Science 316, 1735–1737. http://dx.doi.org/10.1126/science.1136188.
Marshall, D.P., Ambaum, M.H.P., Maddison, J.R., Munday, D.R., Novak, L., 2017. Eddy saturation and frictional control of the antarctic circumpolar current. Geophys. Res. Lett. 44. http://dx.doi.org/10.1002/2016GL071702.
Marshall, D.P., Zanna, L., 2014. A conceptual model of ocean heat uptake under climate change. J. Clim. 27, 8444–8465. http://dx.doi.org/10.1175/JCLI-D-13-00344.1.
Marshall, G.J., 2003. Trends in the southern annular mode from observations and reanalyses. J. Clim. 1, 4134–4143. http://dx.doi.org/10.1175/1520-0442(2003)016<4134:TITSAM>2.0.CO;2.
Marshall, J., Radko, T., 2003. Residual-mean solutions for the antartic circumpolar current and its associated overturning circulation. J. Phys. Oceanogr. 33, 2341–2354. http://dx.doi.org/10.1175/1520-0485(2003)033<2341:RSFTAC>2.0.CO;2.
Marshall, J., Speer, K., 2012. Closure of the meridional overturning circulation through Southern Ocean upwelling. Nat. Geosci. 5, 171–180. http://dx.doi.org/10.1038/NGEO1391.
Mazloff, M.R., 2012. On the sensitivity of the drake passage transport to air-sea momentum flux. J. Clim. 25, 2279–2290. http://dx.doi.org/10.1175/JCLI-D-11-00030.1.
Morrison, A.K., Hogg, A.M., 2013. On the relationship between Southern Ocean overturning and acc transport. J. Phys. Oceanogr. 43, 140–148. http://dx.doi.org/10.1175/JPO-D-12-057.1.
Morrow, R., Ward, M.L., Hogg, A., Pasquet, S., 2010. Eddy response to Southern Ocean climate modes. J. Geophys. Res. 115, C10030. http://dx.doi.org/10.1029/2009JC005894.
Munday, D.R., Johnson, H.L., Marshall, D.P., 2013. Eddy saturation of equilibrated circumpolar currents. J. Phys. Oceanogr. 43, 507–532. http://dx.doi.org/10.1175/JPO-D-12-095.1.
Munk, W.H., Palmén, E., 1951. Note on the dynamics of the antarctic circumpolar current. Tellus 3, 53–55. http://dx.doi.org/10.1111/j.2153-3490.1951.tb00776.x.
Nadeau, L., Straub, D.N., 2009. Basin and channel contributions to a model antarctic circumpolar current. J. Phys. Oceanogr. 39, 986–1002. http://dx.doi.org/10.1175/2008JPO4023.1.
Roberts, M.J., Marshall, D.P., 2000. On the validity of downgradient eddy closures in ocean models. J. Geophys. Res. 105, 28613–28627. http://dx.doi.org/10.1029/1999JC000041.
Sallée, J.B., Speer, K., Morrow, R., 2008. Response of the antarctic circumpolar current to atmospheric variability. J. Clim. 21, 3020–3039. http://dx.doi.org/10.1175/2007JCLI1702.1.
Sigman, D.M., Boyle, E.A., 2000. Glacial/interglacial variations in atmospheric carbon dioxide. Nature 407, 859–869. http://dx.doi.org/10.1038/35038000.
Small, R.J., et al., 2014. A new synoptic scale resolving global climate simulation using the community earth system model. J. Adv. Model. Earth Syst. 6, 1065–1094. http://dx.doi.org/10.1002/2014MS000363.
Smith, R.D., et al., 2010. The Parallel Ocean Program (POP) reference manual, ocean component of the Community Climate System Model (CCSM). Technical Report. Los Alamos National Laboratory.
Steele, M., Morley, R., Ermold, W., 2001. Phc: a global ocean hydrography with a high-quality arctic ocean. J. Clim. 14, 2079–2087. http://dx.doi.org/10.1175/1520-0442(2001)014<2079:PAGOHW>2.0.CO;2.
Tansley, C.E., Marshall, D.P., 2001. On the dynamics of a wind-driven circumpolar current. J. Phys. Oceanogr. 31, 3258–3273. http://dx.doi.org/10.1175/1520-0485(2001)031<3258:OTDOWD>2.0.CO;2.
Thompson, A.F., 2008. The atmospheric ocean: eddies and jets in the antarctic circumpolar current. Philos. Trans. R. Soc. 366, 4529–4541. http://dx.doi.org/10.1098/rsta.2008.0196.
Thompson, A.F., Stewart, A.L., Bischoff, T., 2016. A multi-basin residual-mean model for the global overturning circulation. J. Phys. Oceanogr. 46, 2583–2604. http://dx.doi.org/10.1175/JPO-D-15-0204.1.
Thompson, D.W.J., Solomon, S., 2002. Interpretation of recent southern hemisphere climate change. Science 296, 895–899. http://dx.doi.org/10.1126/science.1069270.
Toggweiler, J.R., Samuels, B., 1995. Effect of drake passage on the global thermohaline circulation. Deep-Sea Res. 42, 477–500. http://dx.doi.org/10.1016/0967-0637(95)00012-U.
Viebahn, J., Eden, C., 2012. Standing eddies in the meridional overturning circulation. J. Phys. Oceanogr. 42, 1486–1508. http://dx.doi.org/10.1175/JPO-D-11-087.1.
Yuan, X., 2004. High-wind-speed evaluation in the Southern Ocean. J. Geophys. Res. 109, D13101. http://dx.doi.org/10.1029/2003JD004179.
Zika, J.D., Sommer, J.L., Dufour, C.O., Garabato, A.N., Blaker, A., 2013. Acceleration of the antarctic circumpolar current by wind stress along the coast of antarctica. J. Phys. Oceanogr. 43, 2772–2784. http://dx.doi.org/10.1175/JPO-D-13-091.1.